



Enhanced cycling stability and rate capability of silicon/graphite anodes by chitosan-based aqueous binder

Jiawei Qi¹ · Xiaobo Yu¹ · Bingshuai Chen¹ · Haitao Zhuo¹ · Shaojun Chen²

Received: 9 October 2022 / Revised: 13 December 2022 / Accepted: 27 December 2022 / Published online: 1 February 2023
© The Author(s), under exclusive licence to Springer-Verlag GmbH Germany, part of Springer Nature 2023

Abstract

Si/Gr anodes have high specific capacity but their cycle stability is not ideal due to excessive volume expansion during discharge/charge cycling, thereby limiting the commercialization of lithium-ion batteries (LIBs). In this paper, a chitosan-polyvinyl alcohol (CS-PVA) water-based binder was prepared. Unlike conventional one-dimensional structural adhesives, CS-PVA adhesives are rich in hydroxyl and amino polar groups. The polar groups induced interactions with Si–OH on silicon particles, further enhancing the structural stability of Si/Gr anode to maintain long-term stable cycling of LIBs. In addition, the Si/Gr anode formed a stable solid electrolyte interface (SEI) during the activation process, leading to long-term stable cycling Si/Gr anodes. The first Coulomb efficiency of Si/Gr@PC11 anode reached 85.5%. And at the current density of 0.5C, the discharge capacity stabilized at 505mAh g⁻¹ after 200 cycles, and reached 433mAh g⁻¹ after 500 cycles. In summary, the success of this work provides a promising avenue to develop high-capacity lithium battery packs with extended cycle life.

Keywords Chitosan · Si/Gr anodes · Aqueous binders · 3D network · Li-ion batteries

Introduction

The binder is an inactive component of the electrode purposed to mainly bind the active material with conductive additive, as well as binds both to the surface of the current collector. In lithium batteries, binders, such as polyvinylidene fluoride (PVDF), are considered non-functional components. However, recent studies have shown that binders greatly influence the cycling stability and capacity retention of batteries [1–4]. In commercial lithium-ion batteries (LIBs), polyvinylidene fluoride (PVDF) is often used as a binder due to its good adhesion and wide electrochemical window. However, the van der Waals forces between PVDF and active species cannot accommodate the huge volume change (300–400%) of silicon particles during charge/

discharge cycling. Meanwhile, PVDF uses N-methyl-2-pyrrolidone (NMP) solvent, which is volatile, flammable, and explosive with a serious impact on the environment [5, 6]. Hence, numerous binders containing reactive groups have been used on silicon-based anodes. Examples include carboxymethyl cellulose (CMC) [7], guar gum [8], karaya gum [9], sodium alginate (Alg) [10], and β -cyclodextrin polymer (β -CDp) [3]. Some studies showed that the reactive groups in such binders can form hydrogen bonds with silicon particles to yield stronger adhesion than PVDF. However, such polymer binders are only one-dimensional structures, prone to sliding of their linear molecular chains slide to result in fall off of the surface of the active material during repeated discharge/charge processes. The three-dimensional (3D) structure effectively buffers the volume expansion of silicon, thereby improving the cycle life of silicon-based anodes [11, 12]. Recently, many 3D cross-linkable polymers including PAA-CMC [13], PAA-PEI [14], CMC-SA [15], and PAA/poly-rotaxane [16] have been explored as binders for Si-based anodes owing to their better mechanical strain resistance, good performance, and strong interaction with silicon particles. However, despite the great progress of binders on silicon-based anodes, relatively few binders have been practically applied to commercial Si/Gr anodes. Therefore,

✉ Haitao Zhuo
haitaozhuo@163.com

¹ College of Chemistry and Environmental Engineering, Shenzhen University, Shenzhen 518060, China

² Shenzhen Key Laboratory of Polymer Science and Technology, College of Materials Science and Engineering, Guangdong Research Center for Interfacial Engineering of Functional Materials, Shenzhen University, Shenzhen 518060, China

developing adhesives for the practical application of Si/Gr anodes is important [17, 18].

Chitosan (CS) is a natural soluble polysaccharide derived from poly(N-acetyl-D-glucosamine) (chitin), mainly composed of β -(1,4)-linked 2-deoxy-2-amino-D-glucopyranose unit. Extensive research has so far been carried out in antibacterial [19], water treatment [20], medical [21], and energy storage [22]. Recently, CS has received extensive attention as an alternative binder in electrodes due to its abundant reactive groups (amino and hydroxyl groups). The first Coulombic efficiency of the PVDF-based graphite electrode has been estimated to 89.3%, while the first Coulombic efficiency of the CS-based graphite electrode has been improved to reach 95.4% [23]. Compared to PVDF-based silicon-based anodes, carboxymethyl chitosan-based silicon-based anodes also showed better cycling stability, with a discharge capacity of 950 mAh g⁻¹ after 50 cycles at a current density of 500 mAh g⁻¹ [24]. In addition, CS-based adhesive systems with cross-linkable groups may be more suitable for LIBs, including CS-(glutaraldehyde) [25], carboxymethyl CS/poly (ethylene oxide) [26], and CS-PAA/PAANa [27]. On the other hand, though these binder systems effectively improve the electrochemical performance, their application in Si/Gr anodes is not suitable due to the complex preparation process and poor adhesion performance. Therefore, exploring novel binder systems suitable for Si/Gr anodes is highly desirable.

PVA is an excellent hydrophilic polymer with good chemical resistance. Its non-toxic and biodegradable properties made it widely used in practical life, including as adhesive in the textile, biomedical, and pharmaceutical industries [28]. PVA can also be easily modified by chemical crosslinking to improve its electrical and thermal properties [29]. In addition, PVA containing large numbers of hydroxyl groups is made of gel polymer electrolytes with good ionic conductivity due to its strong intermolecular and intramolecular interactions with Li ions [30]. However, the one-dimensional structure of PVA is difficult to accommodate the volume expansion of Si particles when used in Si/Gr anodes. When PVA is combined with other polymer binders containing a large number of active groups (-OH, -NH₂), the -OH groups on the PVA group will form dynamic hydrogen bonds with other active groups, thereby forming a three-dimensional network structure, which further promotes the mechanical strength of the binder system [31].

In this work, the PVA-incorporated chitosan network structure was designed to obtain sufficient adhesion and elasticity, further enhancing the structural stability of the Si/Gr anode and enabling batteries with a stable SEI layer during activation. To this end, CS and PVA were mixed at a certain proportion to yield a 3D network water-soluble binder (denoted PC) for Si/Gr anode. Here, CS endowed PC adhesive with strong adhesive ability, and PVA improved the

flexibility of PC adhesive and combined with CS to form dynamic hydrogen bonds. The electrochemical properties of Si/Gr@PVDF, Si/Gr@CS, and Si/Gr@PC anodes were explored by investigating the effect of PC binder on the electrochemical performance of Si/Gr anodes. The Si/Gr anode based on PC11 binder exhibited a reversible capacity of 433 mAh g⁻¹ after 500 cycles at 0.5C, a value significantly higher than those of Si/Gr@PVDF and Si/Gr@CS electrodes. At a super-large rate of 5C, the reversible capacity of Si/Gr@PC11 electrode was tenfold and sevenfold of those of Si/Gr@PVDF and Si/Gr@CS electrodes. Surface SEM images showed that the PC11 anode maintained integrity before and after 100 cycles with little microcracks and delamination.

Experimental section

Materials

Chitosan (Mw = 100–300 kDa) was purchased from J&K Chemical, and polyvinyl alcohol (Mw = 145 kDa) was obtained from Shanghai Aladdin. Silicon/graphite powder (about 6% Si) was received from Shenzhen BTR Nanoscience and Technology Co., Ltd, and Super P (99%) was provided by Alfa Aesar. All chemicals were used as received without further purification.

Preparation of the CS – PVA binders

The preparation consisted of dissolving chitosan in a 2 wt % acetic acid aqueous solution to form a 2 wt % chitosan solution. Next, 5 wt% PVA solution was prepared by dissolving 2 g PVA in 38 g de-ionized water at 95°C. Different amounts of PVA to CS solutions were then designed to configure three CS-PVA mixed solutions with different ratios. The mass ratios of PVA and CS in the three mixed solutions were set to 1:1, 1:2, and 2:1, denoted as PC11, PC12, and PC21, respectively. The PC binder was stirred for 24 h before use and detailed feed composition for preparing the PC adhesive is listed in Table S1.

Characterization

The functional groups on the surface of each sample were characterized by Fourier transform infrared (FT-IR, Nicolet 6700) spectrometry. Differential scanning calorimetry (DSC, Discovery DSC25) analysis was used to determine the samples' glass transition temperature. Thermogravimetric analysis (TGA) experiments were performed on a TA Instruments (TGA Q50) system under N₂ flow (60 mL/min) in the scanning range of 25 to 600 °C and heating rate of 10 °C/min. Peeling tests were carried out on a UTM6103

universal testing machine. To this end, the coated side of each electrode (3×8 cm) was attached to single-sided adhesive tape (2.5×7.5 cm), while the other side was attached to a fixed glass using double-sided adhesive tape. The coating layer peeled off the copper current collector by pulling the single-sided adhesive tape at an angle of 180° with a constant displacement rate of 10 mm/s. X-ray diffraction (XRD) was carried out on an X'Pert Pro MPD X-ray Diffractometer (PANalytical B.V., Holland) using Cu K α radiation (0.15406 nm). Scanning electron microscopy (SEM, JSM-7800F, JEOL, Japan) and energy dispersive spectrometry (EDS) were employed for morphology, structure, and element distribution analyses of commercial silicon/graphite power.

Preparation of electrodes and electrochemical characterization

The electrodes were fabricated by thoroughly mixing silicon/graphite and Super P in an aqueous solution of PC binder at a weight ratio of 8:1:1 under stirring for 12 h. The obtained slurry was then coated on copper foil using a doctor blade, followed by drying in a convection oven for 2 h and a vacuum oven at 120°C overnight. PVDF in NMP and CS dissolved in water was utilized as the control binder. The areal mass loading of each electrode was controlled to approximately 2.0 mg cm^{-2} . In an argon-filled glove box, the electrodes were cut into circular sheets (diameter 14 mm), and their cycling performances were evaluated in CR2032-type coin cells using Li metal as the counter electrode, the polyethylene film (Celgard 2400) as the separator, and 1.0 M LiPF $_6$ in EC/DEC (1:1 by volume) containing 5 wt% FEC as the electrolyte. To assemble coin-type full cells, LiFePO $_4$ cathode was fabricated by preparing a slurry consisting of LiFePO $_4$, super P, and PVDF in a weight ratio of 80:10:10 in NMP. The slurry was cast onto aluminum foil and dried at 70°C for 12 h under a vacuum. The n/p ratio defined by the capacity ratio between the anode and cathode was 1.15. The organic electrolyte of full cells was the same as that of half cells. As for the half cells, galvanostatic charge/discharge tests were recorded on a Neware BTS-81 instrument between 0.01 and 1.5 V (versus Li $^+$ /Li). A low C rate (0.05 C) was used for the first two cycles of activation, followed by cycling tests at 0.5 C (1 C = 600 mAh g^{-1}). As for the full cell, galvanostatic charge/discharge tests were recorded on a Neware BTS-81 instrument between 2 and 4.2 V. A low C rate (0.05 C) was used for the first two cycles of activation, followed by cycling tests at 1 C (1 C = 170 mAh g^{-1}). Electrochemical impedance spectroscopy (EIS) and cyclic voltammetry (CV) measurements were carried out on a 1470E electrochemical workstation (Solartron Analytical). The CV scans were obtained at a scan rate of 0.2 mV s^{-1} in the voltage range of 0.01–1.5 V. The EIS measurements were

performed at an amplitude value of 10 mV and frequencies between 10 mHz and 100 kHz. All EIS fitting data were obtained by ZView software (Scribner Associates, Version 3.5).

Results and discussion

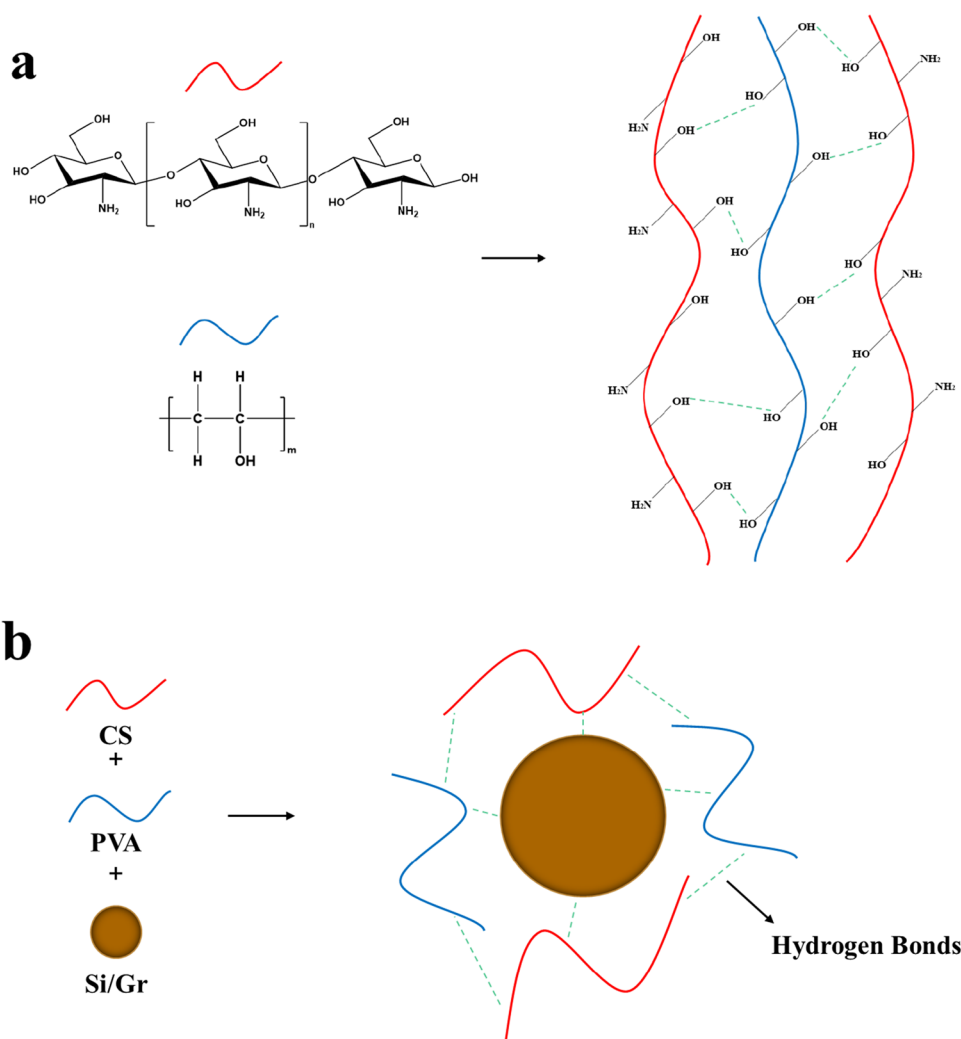
The binding mechanism of CS and PVA binders and that between PC binder and active substances are provided in Fig. 1a–b. The combination of PC binder with the active material formed a strong chemical bond between the active groups -OH and -NH $_2$ with the silicon particles, leading to a tightly combined active material, conductive agent, and binder [32]. This structure well maintained the stability of the Si/Gr anode, enabling withstanding the repeated expansion of silicon particles during long-term cycling [33].

The FTIR spectra of CS, PVA, PC11, PC12, and PC21 are shown in Fig. 2a. The peaks at about 3329, 2889, and 1022 cm^{-1} in the FTIR spectrum of CS were attributed to the stretching vibrations of N–H/O–H, C–H, and C–O, respectively. The peaks at about 1649, 1550, and 1373 cm^{-1} corresponded to the stretching vibration of C–O (amide-I), the in-plane bending vibration of N–H (amide-II), and the stretching vibration of C–N (amide-III), respectively [27]. Compared to CS spectra, both the N–H and O–H peaks in the PC binder system shifted to lower wavenumbers (1548 cm^{-1} and 3283 cm^{-1}), confirming the formation of hydrogen bonds. In addition, the stretching vibration peak intensity of C–O (amide-I) in the PC binder system was greatly reduced, further proving the formation of intermolecular hydrogen bonds [15].

Binders with high crystallinity often impede the flow of electrolyte molecules and increase the resistance of the electrodes, thereby reducing the electrochemical performance of LIBs [34]. Therefore, preparing adhesives with amorphous structures or with low crystallinity is important. The XRD patterns of PVDF, PVA, CS, PC11, PC12, and PC21 are shown in Fig. 2b. PVDF and PVA were crystalline polymers with high crystallinity, while CS was amorphous. The crystallinity of the PC binder containing PVA was significantly lower than that of PVDF. This may reduce the internal impedance of the cell to a certain extent, resulting in good capacity retention. The transition of the PC binder to an amorphous state also further demonstrated the intermolecular interaction between CS and PVA [35]. After XRD measurements, CS and PC binders were found more suitable for LIBs than PVDF.

Better wettability between the binder and the current collector allows for better adherence to the slurry to adhere. The contact angle between each binder and the current collector is shown in Fig. S1. The contact angles of CS, PVDF, PC11, PC12, and PC21 with the current collector were estimated

Fig. 1 **a** The binding mechanism of CS and PVA. **b** Bonding mechanism between PC binder and active substance



to 90.7°, 93.6°, 82.0°, 88.5°, and 71.6°, respectively. The wettability of the PC binder containing PVA improved, conducive to the formation of a tighter bond between the active material, conductive agent, and current collector.

The solubility of PVDF, CS, PC11, PC12, and PC21 films after soaking in the electrolyte for 48 h is displayed in Fig. 2c. Although the polymer films were insoluble in the electrolyte, they swelled more or less after soaking. The swelling rate of CS, PC11, PC12, and PC21 binders after soaking for 48 h was much lower than that of PVDF. Larger swelling ratios of the binder led to a significant increase in electrode thickness, resulting in severe capacity fading and shorter cycle life of LIBs. Therefore, the PC can be used as a binder for Si/Gr anodes.

The thermal properties of the composite adhesive were investigated by DSC and TGA. As shown in Fig. 3a–b, the degradation temperature (T_{10}) values of PC11, PC12, and PC21 were estimated to 255.5, 251.3, and 262.2 °C, respectively. Thus, T_{10} value of PC binder was higher than that of CS (240.3°C), indicating that the introduction of PVA

improved the thermal stability of PC adhesive. As shown in Fig. 3c, the glass transition temperatures (T_g) of PC11, PC12, and PC21 were recorded as 81.7, 88.7, and 72.5 °C, respectively. The T_g of the PC adhesive was lower than that of the CS (106.8 °C), suggesting that the introduction of PVA improved the flexibility of the PC adhesive.

Figure 3d shows the 180° peel test results of Si/Gr electrodes prepared by PVDF, CS, PC11, PC12, and PC21. The mean peel strengths for PVDF, CS, PC11, PC12, and PC21 were estimated to 0.5, 0.97, 1.25, 1.13, and 1.07 N cm⁻¹, respectively. Optical images of all electrodes after peel testing demonstrated better adhesion of the PC binder (Fig. S2). The electrode material on the pole piece prepared with PC binder was hardly peeled off from the copper current collector, while that on the pole piece prepared with CS and PVDF looked largely peeled off. The reason for this had to do with the structural advantages of the physical cross-linking of CS and PVA in PC binders. Moreover, the CS binder formed strong chemical bonds with the surface of the active material, closely combining the active material, conductive

Fig. 2 **a** FTIR spectra of binder films. **b** XRD curves of binder films. **c** Swelling ratios of binder films. **d** Adhesive film soaked in electrolyte

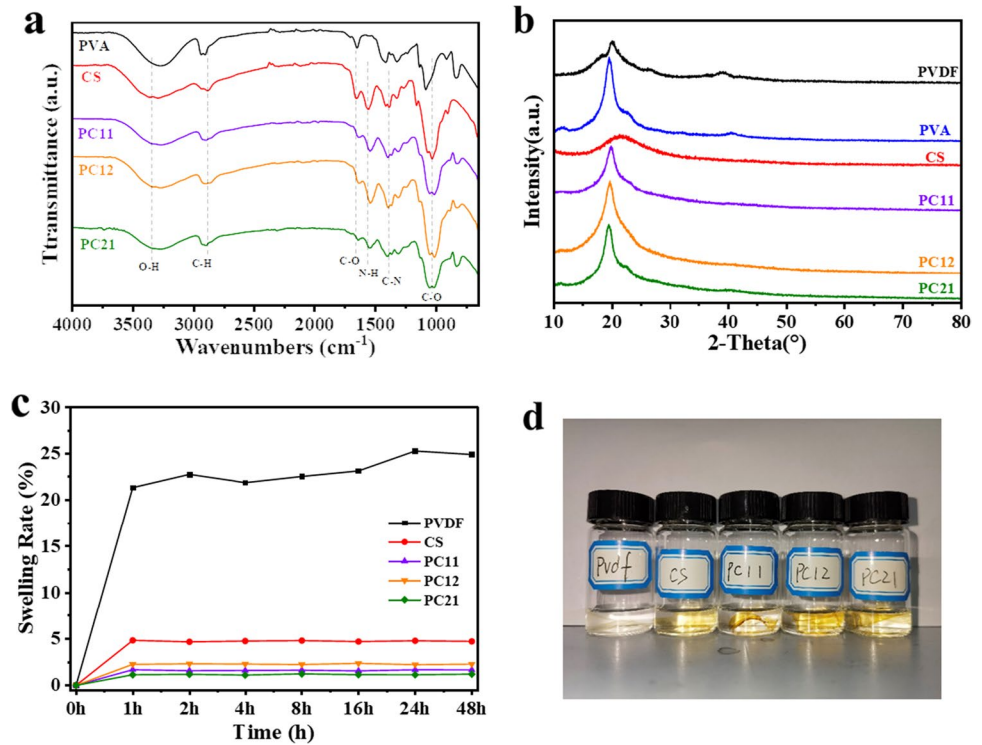
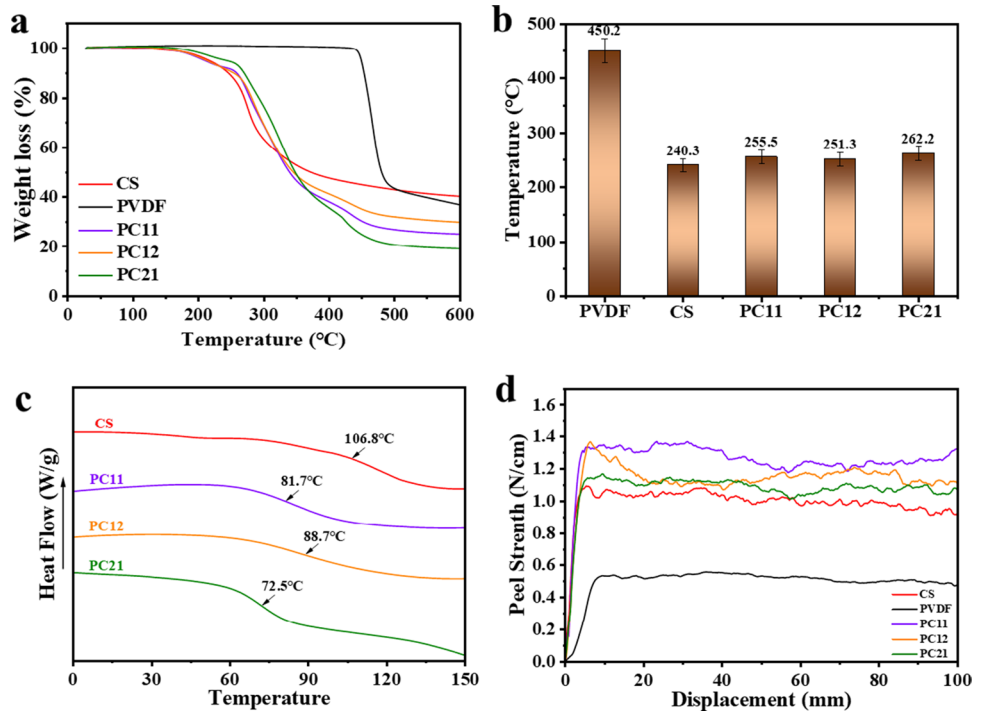


Fig. 3 **a** TGA results of various binders. **b** Thermal decomposition temperature of various binders. **c** DSC curves of binders. **d** Peel strength–displacement curves of Si/Gr anodes fabricated with various binders during 180° peel tests

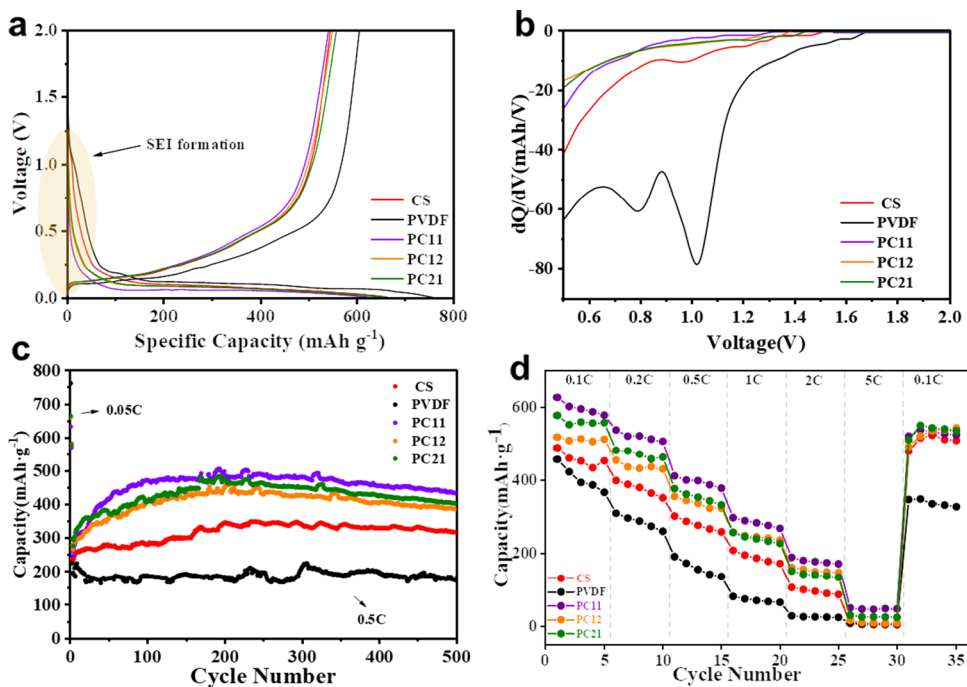


agent, and current collector. As a result, the pole piece prepared by the PC binder possessed a higher mechanical strain resistance.

The XRD, SEM, and EDS patterns of the active material Si/Gr are depicted in Fig. S3. The content of nano-silicon contained in the active material Si/Gr was estimated to 6%.

The electrochemical performances of Si/Gr anodes prepared with each binder were investigated in coin cells. The initial charge–discharge curves of Si/Gr@PVDF, Si/Gr@CS, Si/Gr@PC11, Si/Gr@PC12, and Si/Gr@PC21 anodes at 0.05C are summarized in Fig. 4a. The initial charge/discharge capacities of Si/Gr@PVDF, Si/Gr@CS, Si/Gr@PC11,

Fig. 4 **a** Voltage profiles. **b** dQ/dV plots recorded during the first cycle of each Si/Gr anode obtained with a different binder. **c** Specific discharge capacity. **d** Rate capability performances of Si/Gr anodes obtained with different binders



Si/Gr@PC12, and Si/Gr@PC21 anodes were recorded as 608/762, 544/662, 541/633, 549/660, and 558/665 mAh g^{-1} , respectively. The corresponding initial Coulombic efficiencies were 79.5%, 82.2%, 85.5%, 83.2%, and 83.9%, respectively (Fig. S4). Si/Gr@PC11 anode exhibited the highest reversibility, while the Si/Gr@PVDF anode showed inferior performance due to the formation of a thick SEI layer at the interface between Si/Gr@PVDF anode and electrolyte [36, 37]. The PVDF binder with an extremely strong ability to absorb electrolytes resulted in continuous decomposition of the adsorbed electrolytes to form thick SEI layers. This was confirmed by the dQ/dV curve, where two reduction reaction peaks of the electrolyte appeared at 0.79 and 1.01 V (Fig. 4b) [38, 39]. Meanwhile, the Si/Gr@CS anode exhibited a similar reduction reaction peak at 0.97 V with smaller intensity, indicating the consumption of small amounts of an electrolyte by that CS. The PC11, PC12, and PC21 showed insignificant reduction peaks at 1.25 V, 1.20 V, and 1.25 V when compared to CS and PVDF, respectively. Thus, the introduction of PVA further reduced electrolyte consumption and contributed to the formation of thinner SEI layers.

The cycling performances of Si/Gr anodes prepared with each binder after 500 cycles at 0.5C are shown in Fig. 4c. The relatively large capacity change in the first 100 cycles is may be due to increased electrolyte penetration/electrode activation during battery operation under ultrahigh current density [40, 41]. After 200 cycles, the discharge specific capacity of Si/Gr@PVDF, Si/Gr@CS, Si/Gr@PC11, Si/Gr@PC12, and Si/Gr@PC21 anodes remained around 175, 344, 505, 450, and 476 mAh g^{-1} , respectively. Compared with the discharge specific capacity of the first cycle, their

capacity retention rates were 23.0%, 52.0%, 79.9%, 68.2%, and 71.6%, respectively. After 500 cycles, the discharge specific capacity of Si/Gr@PVDF, Si/Gr@CS, Si/Gr@PC11, Si/Gr@PC12, and Si/Gr@PC21 anodes remained around 173, 316, 433, 386, and 403 mAh g^{-1} , respectively. By contrast, the cycling performance of Si/Gr anodes prepared with all PC binders was improved to some extent. Among electrodes, the Si/Gr@PC11 anode showed the best cycle performance. The Si/Gr@PC11 anode displayed a high discharge capacity of 505 mAh g^{-1} at 200 cycles after the previous activation. And after 500 cycles, its discharge specific capacity is 117 mAh g^{-1} higher than that of Si/Gr@CS anode. Figure S5 shows the Coulombic efficiencies (CE) of Si/Gr@PVDF, Si/Gr@CS, Si/Gr@PC11, Si/Gr@PC12, and Si/Gr@PC21 electrodes during long cycling. The CE of the Si/Gr@PVDF anode fluctuates greatly during cycling. The CE of the Si/Gr@CS anode also fluctuates slightly around 50 cycles. However, the CE of Si/Gr@PC11 electrode remained stable, further demonstrating the superiority of the Si/Gr@PC11 electrode for long cycling. Figure S6 illustrates the long-cycle performance of Si/Gr@PC11 electrode at a current density of 120 mA/g (0.2 C). The discharge specific capacity is stable at 550 mAh g^{-1} after 500 cycles. The rate performances of Si/Gr anodes prepared with various binders were compared at current densities from 0.1 to 5 C and the data are gathered in Fig. 4d. The rate capability of Si/Gr anode using PC binder looked better than those of Si/Gr@PVDF and Si/Gr@CS anodes. The Si/Gr@PC11 anode exhibited the best capacity under all rate conditions. After charging and discharging at different rates, the discharge capacity of Si/Gr@PC11 anode recovered to 90.8% of the

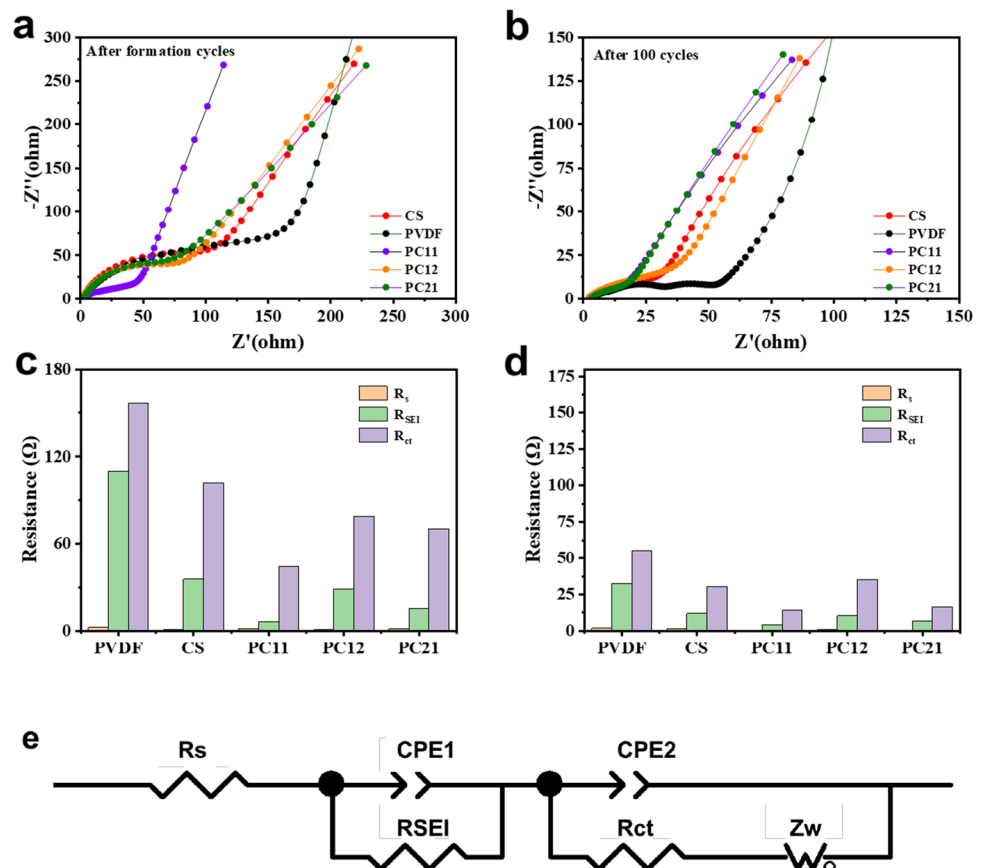
initial value, with discharge capacity reaching 48 mAh g⁻¹ at a high rate of 5C. By comparison, Si/Gr@PVDF and Si/Gr@CS anodes only recorded 4.5 mAh g⁻¹ and 7 mAh g⁻¹, respectively. Therefore, introducing an appropriate amount of PVA into the CS binder improved the long-term cycling performance and rate capability of Si/Gr anodes. The electrochemical performances of the prepared PC11 binder were compared with those of some reported binders (Table S2) and the results showed that PC11 binder system exhibited better long-term cycling stability.

Besides, the coin-type full cells were prepared by pairing the Si/Gr@PC11, anode with a LiFePO₄ (LFP) cathode. The negative/positive (n/p) ratio of the coin-type full cells was set to 1.15. The LFP cathode in full cell delivers a specific capacity of 151 mAh g⁻¹ in the initial activation cycle at 0.05 C (1 C = 170 mAh g⁻¹). Even though full cell undergoes a seriously irreversible process in the initial cycle for the growth of SEI film, its ICE is still as high as 79.2%, which demonstrates the superior role of PC11 binder in the full cell system (Fig. S7b). After the initial two activation cycles, full cell delivers a specific discharge capacity of 149 mAh g⁻¹ in the first cycle at 1 C (1C = 170 mAh g⁻¹) with the CE of 99.8% (Fig. S7a). Moreover, the full cell demonstrates decent cyclability of 50 cycles with an average CE of

99.85% (Fig. S7a). Thus, the PC11 binder has great potential for commercial application.

In dQ/dV diagram (Fig. 4b), the electrochemical performance of Si/Gr anode may be related to the formation of SEI. Therefore, the formation of SEI was further investigated by EIS. Figure 5a–b provides the Nyquist plots of different anodes after 2 cycles at 0.05C and 100 cycles at 1.0C. In the EIS diagram, R_s represents the bulk resistance from the electrolyte and current collector, while the two semicircles from high frequency to medium frequency are attributed to SEI resistance (R_{SEI}) and charge transfer resistance (R_{ct}), respectively. The slope at low frequency represents the Li⁺ diffusion resistance (Z_w) through the porous anode [42, 43]. The initial R_{ct} values of Si/Gr@PVDF, Si/Gr@CS, Si/Gr@PC11, Si/Gr@PC12, and Si/Gr@PC21 electrodes were calculated according to the equivalent circuit (Fig. 5e). As shown in Fig. 5c–d, the initial R_{ct} of the latter four electrodes was significantly lower than that of Si/Gr@PVDF electrode since the amorphous polymer binders were more effective in promoting charge transfer at the electrode/electrolyte interface. After 100 cycles, the R_{ct} value of each electrode decreased, and that of Si/Gr@PC11 was the lowest. The reason for this may have to do with the proper introduction of PVA to facilitate the rapid formation of a stable SEI layer on the Si/Gr

Fig. 5 **a** Nyquist plots of various Si/Gr anodes after two formation cycles at 0.05 C. **b** Nyquist plots of various Si/Gr anodes after 100 cycles at 1 C. **c** Resistance values of various Si/Gr anodes after two formation cycles at 0.05 C. **d** Resistance values of various Si/Gr anodes after 100 cycles at 1 C. **e** Equivalent circuit model for EIS fitting



surface to keep a stable conductive network and structure. This, in turn, declined the charge transfer resistance of the Si/Gr anode.

The electrochemical stabilities of Si/Gr@CS, Si/Gr@PVDF, Si/Gr@PC11, Si/Gr@PC12, and Si/Gr@PC21 electrodes were investigated by CV and the data are shown in Fig. 6a–e. In the third, fourth, fifth, and sixth cycles of the Si/Gr@PVDF electrode, distinct reduction peaks (~ 0.10 V), and corresponding delithiation peaks (~ 0.33 V, 0.53 V) appeared. However, the CV curves of the other four electrodes showed different shapes, with a relatively broad delithiation peak at 0.37 V and a less obvious reduction peak around 0.1 V. This may be related to the formation of SEI film on the Si/Gr anode surface [44–46]. The good

repeatability of the CV curves after the first cycle further indicated the improved electrochemical performances of Si/Gr@PC11, Si/Gr@PC12, and Si/Gr@PC21 electrodes [47, 48].

The morphologies of the newly fabricated and cycled Si/Gr anodes were characterized by SEM. As shown in Fig. 7a–b. The flake graphite before cycling was uniformly covered by silicon nanoparticles, and no cracks were observed on the anode surface. Hence, the morphology of Si/Gr anode prepared with each binder was uniform and complete. After 100 cycles, many deep cracks appeared on the surfaces of Si/Gr@PVDF and Si/Gr@CS anodes (Fig. 7b), suggesting the Si/Gr@PVDF and Si/Gr@CS anodes inability to adapt to the drastic volume change of Si nanoparticles

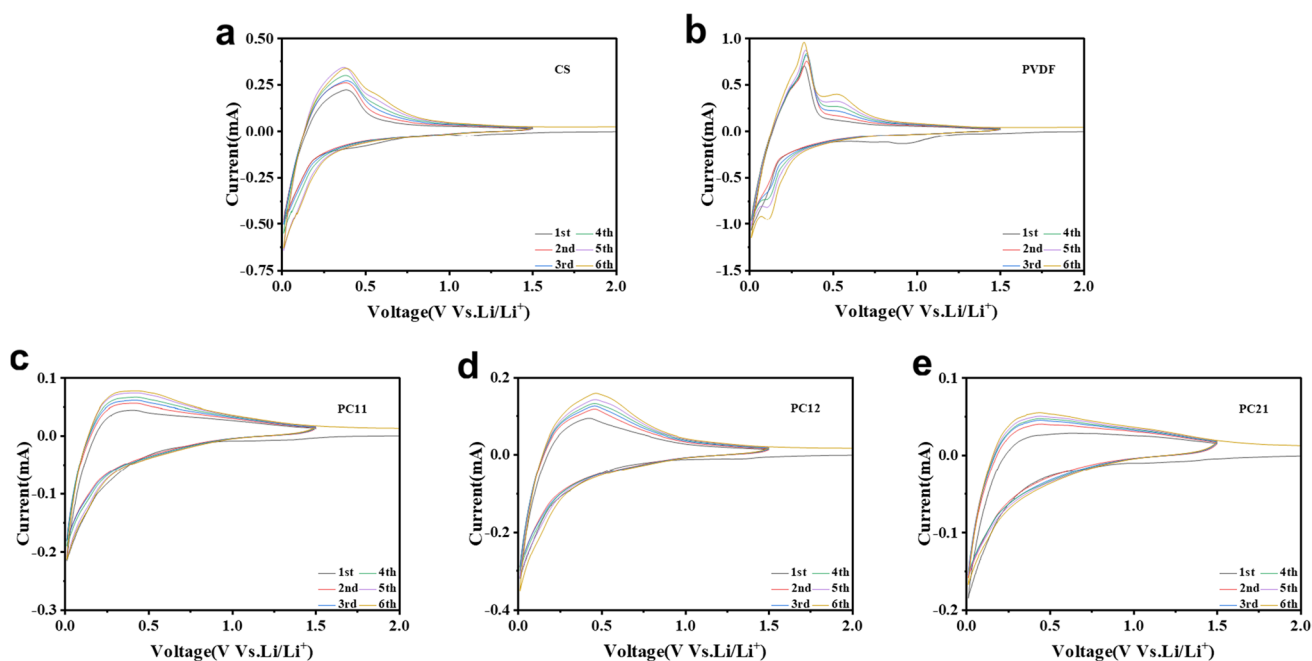


Fig. 6 A–E Cyclic voltammetry plots of various polymer-bonded Si/Gr anodes at a scan rate of 0.2 mV s^{-1}

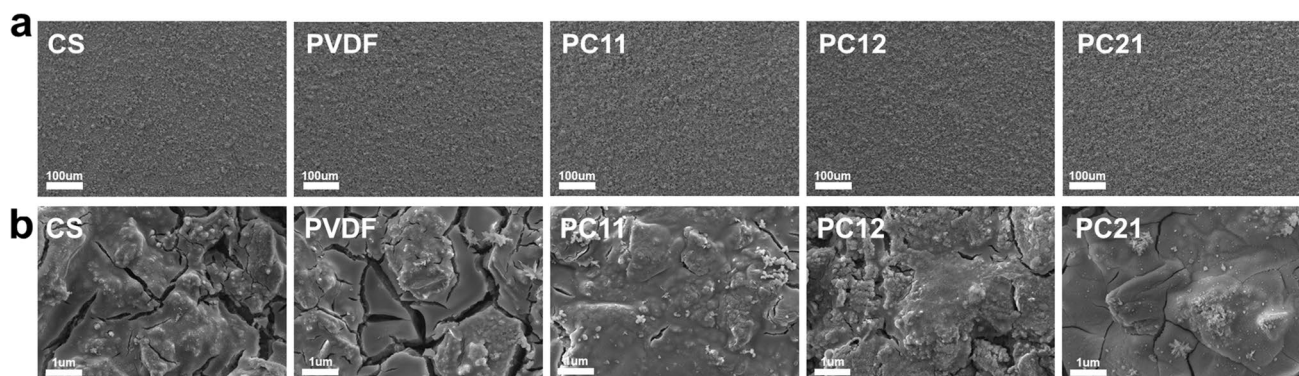


Fig. 7 SEM images of various polymer binder-bonded Si/Gr anodes: **a** before and **b** after 100 cycles

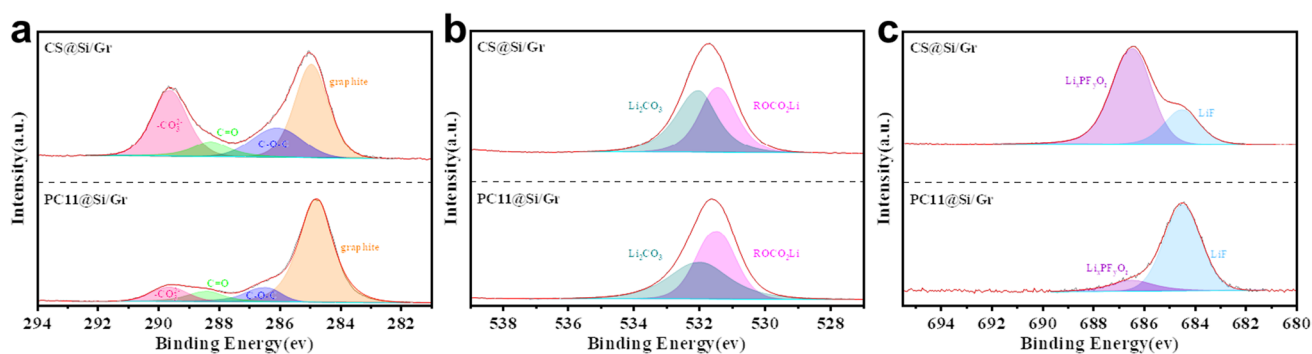


Fig. 8 **a** C 1 s, **b** O 1 s, and **c** F 1 s XPS spectra of Si/Gr@CS and Si/Gr@PC11 anodes after 100 cycles

during long-term cycling. This would explain their poor cycling performance and large electrode impedance. By contrast, the Si/Gr@PC11, Si/Gr@PC12, and Si/Gr@PC21 anodes showed only small amounts of cracks, and Si/Gr@PC11 performed the best. Thus, the physical cross-linked structure of PC binder effectively maintained the structural stability of the Si/Gr anode, leading to improved long-term cycle stability of the electrode.

An ideal binder should contribute to constructing a stable solid-electrolyte interphase (SEI) on Si/Gr anode materials. Thus, electrode surfaces were wrapped with binders in the pristine state, then covered with SEI layers after cycling. To gain a better understanding of the effect of binders on the formation of the SEI layer, XPS was carried out, and Fig. 8 shows the high-resolution spectra of the C 1 s, O 1 s, and F 1 s. Characteristic peaks of C–C (284.8 eV), C–O–C (286.5 eV), and C=O (288.4 eV) are observed in Fig. 8a [49]. An additional peak at 289.6 eV was noticed, attributed to the formed SEI layer components, such as carbonate (Li_2CO_3) [50]. Comparison of C 1 s spectra of Si/Gr@PC11 electrodes with that of Si/Gr@CS electrodes showed a decline in the intensity of the peak corresponding to the SEI layer components for Si/Gr@PC11 electrodes. Thus, the Si/Gr@PC11 electrode had a thinner SEI layer since PC11 binder was well coated onto Si/Gr particle's surface, which inhibited parasitic reactions at the (Si/Gr)/electrolyte interface. This result was also verified by O 1 s spectra (Fig. 8b). After 100 cycles, the spectra of both electrodes showed a significant difference due to the formation of SEI layer. Typical SEI species of ROCO_2Li (531.5 eV) and Li_2CO_3 (532.1 eV) were detected. The relative ratio of the Li_2CO_3 peak intensity in Si/Gr@PC11 electrode was smaller than that of Si/Gr@CS electrode, consistent with the above observation from C 1 s. The F 1 s spectrum is shown in Fig. 8c. After 100 cycles, the electrodes displayed a peak at 684.5 eV linked to LiF, and another peak at 686.5 eV related to $\text{Li}_x\text{PF}_y\text{O}_z$. Importantly, the LiF peak intensity was strong in Si/Gr@PC11 electrode. LiF, as an effective passivation layer, may have a low Li ion diffusion barrier. Thus,

the higher-LiF-containing SEI layers in the Si/Gr@PC11 electrodes could be more ionically conductive to stabilize the electrodes [51].

Conclusions

The design, preparation, and performance of the aqueous binder CS-PVA as Si/Gr anode binder in LIBs were studied. The following conclusions can be drawn: the physically cross-linkable reactive groups facilitated the formation of a robust 3D network of the binder inside the Si/Gr anode, suppressing the volume expansion of silicon nanoparticles in the Si/Gr anode. This also ensured the integrity of the electrode after long-term cycling, as well as improved the electrochemical performance of the Si/Gr anode. The first Coulomb efficiency of Si/Gr@PC11 electrode reached 85.5%. And at the current density of 0.5C, the discharge capacity stabilized at 505mAh g^{-1} after 200 cycles, and reached 433mAh g^{-1} after 500 cycles, a value significantly higher than those of Si/Gr@PVDF and Si/Gr@CS electrodes. At a super-large rate of 5C, the reversible capacity of Si/Gr@PC11 electrode was tenfold and sevenfold of those of Si/Gr@PVDF and Si/Gr@CS electrodes. The excellent long-term cycling stability and high-rate performance of PC11-based Si/Gr anodes and low cost and facile preparation of PC11 binder suggested PC11 as a promising binder for Si/Gr anodes in Li-ion batteries.

Supplementary Information The online version contains supplementary material available at <https://doi.org/10.1007/s11581-022-04877-w>.

Funding This research was supported by the Guangdong Basic and Applied Basic Research Foundation (Grant No. 2022A1515011985), the Shenzhen Science and Technology Planning Project (Grant No. JCYJ20190808115609663), and the Scientific Research Project of Guangdong Provincial Department of Education (Grant No. 2020ZDZX2040).

Declarations

Competing interests The authors declare no competing interests.

References

1. He J, Wei YQ, Hu LT, Li HQ, Zhai TY (2018) Aqueous binder enhanced high-performance GeP5 anode for lithium-ion batteries. *Front Chem* 6:10. <https://doi.org/10.3389/fchem.2018.00021>
2. Jeong SS, Bockenfeld N, Balducci A, Winter M, Passerini S (2012) Natural cellulose as binder for lithium battery electrodes. *J Power Sources* 199:331–335. <https://doi.org/10.1016/j.jpowsour.2011.09.102>
3. Jeong YK, Kwon TW, Lee I, Kim TS, Coskun A, Choi JW (2014) Hyperbranched beta-cyclodextrin polymer as an effective multidimensional binder for silicon anodes in lithium rechargeable batteries. *Nano Lett* 14(2):864–870. <https://doi.org/10.1021/nl404237j>
4. Lim S, Lee K, Shin I, Tron A, Mun J, Yim T et al (2017) Physically cross-linked polymer binder based on poly(acrylic acid) and ion-conducting poly(ethylene glycol-co-benzimidazole) for silicon anodes. *J Power Sources* 360:585–592. <https://doi.org/10.1016/j.jpowsour.2017.06.049>
5. Li J-T, Wu Z-Y, Lu Y-Q, Zhou Y, Huang Q-S, Huang L et al (2017) Water soluble binder, an electrochemical performance booster for electrode materials with high energy density. *Advanced Energy Materials*. 7(24):1701185. <https://doi.org/10.1002/aenm.201701185>
6. Song J, Zhou M, Yi R, Xu T, Gordin ML, Tang D et al (2014) Interpenetrated gel polymer binder for high-performance silicon anodes in lithium-ion batteries. *Adv Func Mater* 24(37):5904–5910. <https://doi.org/10.1002/adfm.201401269>
7. Vogl US, Das PK, Weber AZ, Winter M, Kostecki R, Lux SF (2014) Mechanism of interactions between CMC binder and Si single crystal facets. *Langmuir* 30(34):10299–10307. <https://doi.org/10.1021/la501791q>
8. Liu J, Zhang Q, Zhang T, Li J-T, Huang L, Sun S-G (2015) A robust ion-conductive biopolymer as a binder for Si anodes of lithium-ion batteries. *Adv Func Mater* 25(23):3599–3605. <https://doi.org/10.1002/adfm.201500589>
9. Bie Y, Yang J, Nuli Y, Wang J (2017) Natural karaya gum as an excellent binder for silicon-based anodes in high-performance lithium-ion batteries. *J Materials Chem A* 5(5):1919–1924. <https://doi.org/10.1039/c6ta09522d>
10. Kovalenko I, Zdyrko B, Magasinski A, Hertzberg B, Milicev Z, Burtovyy R et al (2011) A major constituent of brown algae for use in high-capacity Li-ion batteries. *Science* 334(6052):75–79. <https://doi.org/10.1126/science.1209150>
11. Ryou MH, Kim J, Lee I, Kim S, Jeong YK, Hong S et al (2013) Mussel-inspired adhesive binders for high-performance silicon nanoparticle anodes in lithium-ion batteries. *Adv Mater* 25(11):1571–1576. <https://doi.org/10.1002/adma.201203981>
12. Zhang GZ, Yang Y, Chen YH, Huang J, Zhang T, Zeng HB et al (2018) A quadruple-hydrogen-bonded supramolecular binder for high-performance silicon anodes in lithium-ion batteries. *Small* 14(29):10. <https://doi.org/10.1002/smll.201801189>
13. Koo B, Kim H, Cho Y, Lee KT, Choi NS, Cho J (2012) A highly cross-linked polymeric binder for high-performance silicon negative electrodes in lithium ion batteries. *Angew Chem-Int Edit* 51(35):8762–8767. <https://doi.org/10.1002/anie.201201568>
14. Chuang YP, Lin YL, Wang CC, Hong JL (2021) Dual cross-linked polymer networks derived from the hyperbranched poly(ethyleneimine) and poly(acrylic acid) as efficient binders for silicon anodes in lithium-ion batteries. *Acs Applied Energy Materials* 4(2):1583–1592. <https://doi.org/10.1021/acsaem.0c02802>
15. Guo RN, Zhang SL, Ying HJ, Yang WT, Wang JL, Han WQ (2019) Preparation of an amorphous cross-linked binder for silicon anodes. *Chemsuschem* 12(21):4838–4845. <https://doi.org/10.1002/cssc.201902079>
16. Choi S, Kwon TW, Coskun A, Choi JW (2017) Highly elastic binders integrating polyrotaxanes for silicon microparticle anodes in lithium ion batteries. *Science* 357(6348):279–283. <https://doi.org/10.1126/science.aal4373>
17. Cao PF, Naguib M, Du ZJ, Stacy E, Li BR, Hong T et al (2018) Effect of binder architecture on the performance of silicon/graphite composite anodes for lithium ion batteries. *ACS Appl Mater Interfaces* 10(4):3470–3478. <https://doi.org/10.1021/acsami.7b13205>
18. Lee SH, Lee JH, Nam DH, Cho M, Kim J, Chanthad C et al (2018) Epoxidized natural rubber/chitosan network binder for silicon anode in lithium-ion battery. *ACS Appl Mater Interfaces* 10(19):16449–16457. <https://doi.org/10.1021/acsami.8b01614>
19. Agnihotri S, Mukherji S, Mukherji S (2012) Antimicrobial chitosan-PVA hydrogel as a nanoreactor and immobilizing matrix for silver nanoparticles. *Appl Nanosci* 2(3):179–188. <https://doi.org/10.1007/s13204-012-0080-1>
20. Pakdel PM, Peighambaroust SJ (2018) Review on recent progress in chitosan-based hydrogels for wastewater treatment application. *Carbohydr Polym* 201:264–279. <https://doi.org/10.1016/j.carbpol.2018.08.070>
21. Chen HL, Cheng JW, Ran LX, Yu K, Lu BT, Lan GQ et al (2018) An injectable self-healing hydrogel with adhesive and antibacterial properties effectively promotes wound healing. *Carbohydr Polym* 201:522–531. <https://doi.org/10.1016/j.carbpol.2018.08.090>
22. Ling Z, Wang G, Zhang MD, Fan XM, Yu C, Yang J et al (2015) Boric acid-mediated B, N-codoped chitosan-derived porous carbons with a high surface area and greatly improved supercapacitor performance. *Nanoscale* 7(12):5120–5125. <https://doi.org/10.1039/c5nr00081e>
23. Chai LL, Qu QT, Zhang LF, Shen M, Zhang L, Zheng HH (2013) Chitosan, a new and environmental benign electrode binder for use with graphite anode in lithium-ion batteries. *Electrochim Acta* 105:378–383. <https://doi.org/10.1016/j.electacta.2013.05.009>
24. Yue L, Zhang L, Zhong H (2014) Carboxymethyl chitosan: a new water soluble binder for Si anode of Li-ion batteries. *J Power Sources* 247:327–331. <https://doi.org/10.1016/j.jpowsour.2013.08.073>
25. Chen C, Lee SH, Cho M, Kim J, Lee Y (2016) Cross-linked chitosan as an efficient binder for Si anode of Li-ion batteries. *ACS Appl Mater Interfaces* 8(4):2658–2665. <https://doi.org/10.1021/acsami.5b10673>
26. Zhong HX, Lu JD, He AQ, Sun MH, He JR, Zhang LZ (2017) Carboxymethyl chitosan/poly(ethylene oxide) water soluble binder: challenging application for 5 V LiNi05Mn1.5O4 cathode. *J Mater Sci Technol* 33(8):763–7. <https://doi.org/10.1016/j.jmst.2017.01.019>
27. Gao Y, Qiu XT, Wang XL, Gu AQ, Zhang L, Chen XC et al (2019) Chitosan-g-poly(acrylic acid) copolymer and its sodium salt as stabilized aqueous binders for silicon anodes in lithium-ion batteries. *Acs Sustainable Chem & Engineering* 7(19):16274–16283. <https://doi.org/10.1021/acssuschemeng.9b03307>
28. Kumar GV, Chandramani R (2009) Investigations on Fe3+ doped polyvinyl alcohol films with and without gamma (γ)-irradiation. *Appl Surf Sci* 255(15):7047–7050. <https://doi.org/10.1016/j.apsusc.2009.03.038>
29. Senel M, Bozkurt A, Baykal A (2007) An investigation of the proton conductivities of hydrated poly(vinyl alcohol)/boric acid complex electrolytes. *Ionics* 13(4):263–266. <https://doi.org/10.1007/s11581-007-0100-4>
30. Hu SM, Wang LDY, Huang T, Yu AS (2020) A conductive self-healing hydrogel binder for high-performance silicon anodes in

- lithium-ion batteries. *J Power Sources* 449:8. <https://doi.org/10.1016/j.jpowsour.2019.227472>
31. Li YX, Fang X, Wang Y, Ma BH, Sun JQ (2016) Highly transparent and water-enabled healable antifogging and frost-resisting films based on poly(vinyl alcohol)-nafion complexes. *Chem Mater* 28(19):6975–6984. <https://doi.org/10.1021/acs.chemmater.6b02684>
 32. Tang R, Ma L, Zhang Y, Zheng X, Shi Y, Zeng X et al (2020) A flexible and conductive binder with strong adhesion for high performance silicon-based lithium-ion battery anode. *ChemElectroChem* 7(9):1992–2000. <https://doi.org/10.1002/celec.201902152>
 33. Nguyen VC, Huynh TKN (2014) Reusable nanocomposite of CoFe₂O₄/chitosan-graft-poly(acrylic acid) for removal of Ni(II) from aqueous solution. *Adv Nat Sci-Nanosci Nanotechnol* 5(2):7. <https://doi.org/10.1088/2043-6262/5/2/025007>
 34. Choi SJ, Yim T, Cho W, Mun J, Jo YN, Kim KJ et al (2016) Rosin-embedded poly(acrylic acid) binder for silicon/graphite negative electrode. *ACS Sustainable Chem Engineering* 4(12):6362–6370. <https://doi.org/10.1021/acssuschemeng.6b00920>
 35. Chen YN, Peng L, Liu T, Wang Y, Shi S, Wang H (2016) Poly(vinyl alcohol)-tannic acid hydrogels with excellent mechanical properties and shape memory behaviors. *ACS Appl Mater Interfaces* 8(40):27199–27206. <https://doi.org/10.1021/acsami.6b08374>
 36. Zhang XR, Kostecki R, Richardson TJ, Pugh JK, Ross PN (2001) Electrochemical and infrared studies of the reduction of organic carbonates. *J Electrochem Soc* 148(12):A1341–A1345. <https://doi.org/10.1149/1.1415547>
 37. Zhuang GV, Yang H, Blizanac B, Ross PN (2005) A study of electrochemical reduction of ethylene and propylene carbonate electrolytes on graphite using ATR-FTIR spectroscopy. *Electrochem Solid State Lett* 8(9):A441–A445. <https://doi.org/10.1149/1.1979327>
 38. Hou TZ, Yang G, Rajput NN, Self J, Park SW, Nanda J et al (2019) The influence of FEC on the solvation structure and reduction reaction of LiPF₆/EC electrolytes and its implication for solid electrolyte interphase formation. *Nano Energy* 64:13. <https://doi.org/10.1016/j.nanoen.2019.103881>
 39. Yohannes YB, Lin SD, Wu NL (2017) In situ DRIFTS analysis of solid electrolyte interphase of Si-based anode with and without fluoroethylene carbonate additive. *J Electrochem Soc* 164(14):A3641–A3648. <https://doi.org/10.1149/2.0681714jes>
 40. Li Z, Zhang Y, Liu T, Gao X, Li S, Ling M et al (2020) Silicon anode with high initial coulombic efficiency by modulated trifunctional binder for high-areal-capacity lithium-ion batteries. *Advanced Energy Materials*. 10(20):1903110. <https://doi.org/10.1002/aenm.201903110>
 41. Liu J, Galpaya DGD, Yan LJ, Sun MH, Lin Z, Yan C et al (2017) Exploiting a robust biopolymer network binder for an ultrahigh-areal-capacity Li-S battery. *Energy Environ Sci* 10(3):750–755. <https://doi.org/10.1039/c6ee03033e>
 42. Shobukawa H, Alvarado J, Yang YYC, Meng YS (2017) Electrochemical performance and interfacial investigation on Si composite anode for lithium ion batteries in full cell. *J Power Sources* 359:173–181. <https://doi.org/10.1016/j.jpowsour.2017.05.044>
 43. Su MR, Wang ZX, Guo HJ, Li XH, Huang SL, Xiao W et al (2014) Enhancement of the cyclability of a Si/graphite@graphene composite as anode for lithium-ion batteries. *Electrochim Acta* 116:230–236. <https://doi.org/10.1016/j.electacta.2013.10.195>
 44. Jiang Y, Mu DB, Chen S, Wu BR, Cheng KL, Li LY et al (2016) Electrochemical performance of Si anode modified with carbonized gelatin binder. *J Power Sources* 325:630–636. <https://doi.org/10.1016/j.jpowsour.2016.06.089>
 45. Lin HY, Li CH, Wang DY, Chen CC (2016) Chemical doping of a core-shell silicon nanoparticles@polyaniline nanocomposite for the performance enhancement of a lithium ion battery anode. *Nanoscale* 8(3):1280–1287. <https://doi.org/10.1039/c5nr07152f>
 46. Liu D, Zhao Y, Tan R, Tian LL, Liu YD, Chen HB et al (2017) Novel conductive binder for high-performance silicon anodes in lithium ion batteries. *Nano Energy* 36:206–212. <https://doi.org/10.1016/j.nanoen.2017.04.043>
 47. Chen D, Yi R, Chen SR, Xu T, Gordin ML, Wang DH (2014) Facile synthesis of graphene-silicon nanocomposites with an advanced binder for high-performance lithium-ion battery anodes. *Solid State Ion* 254:65–71. <https://doi.org/10.1016/j.ssi.2013.11.020>
 48. Zhang ZG, Jiang Y, Peng Z, Yang SS, Lin H, Liu M et al (2017) Facile pyrolyzed N-doped binder network for stable Si anodes. *ACS Appl Mater Interfaces* 9(38):32775–32781. <https://doi.org/10.1021/acsami.7b10314>
 49. Verma P, Maire P, Novak P (2010) A review of the features and analyses of the solid electrolyte interphase in Li-ion batteries. *Electrochim Acta* 55(22):6332–6341. <https://doi.org/10.1016/j.electacta.2010.05.072>
 50. Tang Y, Deng J, Li W, Malyi OI, Zhang Y, Zhou X et al (2017) Water-soluble sericin protein enabling stable solid-electrolyte interphase for fast charging high voltage battery electrode. *Adv Mater*. 29(33):1701828. <https://doi.org/10.1002/adma.201701828>
 51. Wu S, Yang Y, Liu C, Liu T, Zhang Y, Zhang B et al (2020) In-situ polymerized binder: a three-in-one design strategy for all-integrated SiO_x anode with high mass loading in lithium ion batteries. *ACS Energy Lett* 6(1):290–297. <https://doi.org/10.1021/acsenerylett.0c02342>

Publisher's Note Springer Nature remains neutral with regard to jurisdictional claims in published maps and institutional affiliations.

Springer Nature or its licensor (e.g. a society or other partner) holds exclusive rights to this article under a publishing agreement with the author(s) or other rightsholder(s); author self-archiving of the accepted manuscript version of this article is solely governed by the terms of such publishing agreement and applicable law.